Magnetotransport and Spin-Relaxation Signatures of the Radial Rashba and Dresselhaus Spin-Orbit Coupling in Proximitized Graphene

Wun-Hao Kang (康文豪),[1,2] Michael Barth,[3] Andreas Costa,[3] Aitor Garcia-Ruiz,[1,4] Alina Mreńca-Kolasińska,[5] Ming-Hao Liu (劉明豪),[1,2,*] and Denis Kochan[6,2,†]

[1]*Department of Physics, National Cheng Kung University, Tainan 70101, Taiwan*
[2]*Center for Quantum Frontiers of Research and Technology (QFort), National Cheng Kung University, Tainan 70101, Taiwan*
[3]*Institute for Theoretical Physics, University of Regensburg, 93040 Regensburg, Germany*
[4]*National Graphene Institute, University of Manchester, M13 9PL Manchester, United Kingdom*
[5]*AGH University, Faculty of Physics and Applied Computer Science, 30-059 Kraków, Poland*
[6]*Institute of Physics, Slovak Academy of Sciences, 84511 Bratislava, Slovakia*

(Received 29 February 2024; revised 3 August 2024; accepted 4 October 2024; published 19 November 2024)

Graphene-based van der Waals heterostructures take advantage of tailoring spin-orbit coupling (SOC) in the graphene layer by the proximity effect. At long wavelength—saddled by the electronic states near the Dirac points—the proximitized features can be effectively modeled by the Hamiltonian involving novel SOC terms and allow for an admixture of the tangential and radial spin-textures—by the so-called *Rashba angle* θ_R. Taking such effective models we perform realistic large-scale magnetotransport calculations—transverse magnetic focusing and Dyakonov-Perel spin relaxation—and show that there are unique qualitative and quantitative features allowing for an unbiased experimental disentanglement of the conventional Rashba SOC from its novel radial counterpart, called here the *radial Rashba SOC*. Along with that, we propose a scheme for a direct estimation of the Rashba angle by exploring the magneto response symmetries when swapping an in-plane magnetic field. To complete the story, we analyze the magneto-transport and spin-relaxation signatures in the presence of an emergent *Dresselhaus SOC* and also provide some generic ramifications about possible scenarios of the *radial superconducting diode effect*.

DOI: 10.1103/PhysRevLett.133.216201

Graphene-based van der Waals heterostructures provide an ideal platform for exploring various physical phenomena [1–5] that are intertwining single-particle and many-body properties, including magnetic, ferro-electric, topological, and even superconducting states of matter [6–12]. A key ingredient for mediating many of these features is spin-orbit coupling (SOC). Although the latter is small in pristine graphene [13,14], it can be substantially enhanced by proximity effects of either adatoms or other layers [15–37]. The strong SOC can be achieved by proximitizing graphene with transition metal dichalcogenides. A further interplay of twisting, stacking and of long supercell periodicities allows one to engineer and tune the strengths of valley-Zeeman (VZ) and Rashba SOC [21,25,38–46].

The new kid on the block is a possibility to engender the Rashba SOC with a radial component. As shown in [47], there are very specific twist angles allowing for pure radial Rashba (RR) SOC. However, in general, the resulting spin texture admixes both [9,48,49], the tangential and radial components, quantified by a Rashba angle θ_R, and as such it gives rise to a tilted spin-momentum locking triggering, for example, unconventional spin-to-charge conversion [43,44,48]. These novel spin textures are going beyond the ordinary SOC classification based on a reduction of just the graphene-point group symmetries [27]. Indeed, the long-wavelength electronic states with momenta near the valley centers experience a much more complex interaction landscape and the inherent supercell symmetries differ from ordinary graphene allowing for more complex SOC Hamiltonians [40,41].

This Letter has three primary goals: (i) to identify robust magnetotransport signatures allowing for experimentally unique discrimination between the conventional Rashba (CR) and RR SOC, and also for the determination of their admixing Rashba angle θ_R; (ii) in addition to CR and RR, to explore also the spintronics consequences of the Dresselhaus SOC [50], even though there are not yet reported experimental, neither DFT evidences of the presence of a Dresselhaus term in graphene, nevertheless the existing rush in the field can not preclude its exposure in near future; (iii) apart from graphene, to examine also emergent magnetochiral responses of the superconducting diode effect (SDE) in a proximitized two-dimensional electron gas (2DEG) whose spin texture follows RR, CR (or their admixture), and/or Dresselhaus SOC.

Rationale: Spin textures vs in-plane magnetosymmetries—Why the spin textures matter for magnetosymmetry responses can be seen from Figs. 1(a)–1(d), showing

*Contact author: minghao.liu@phys.ncku.edu.tw
†Contact author: denis.kochan@savba.sk

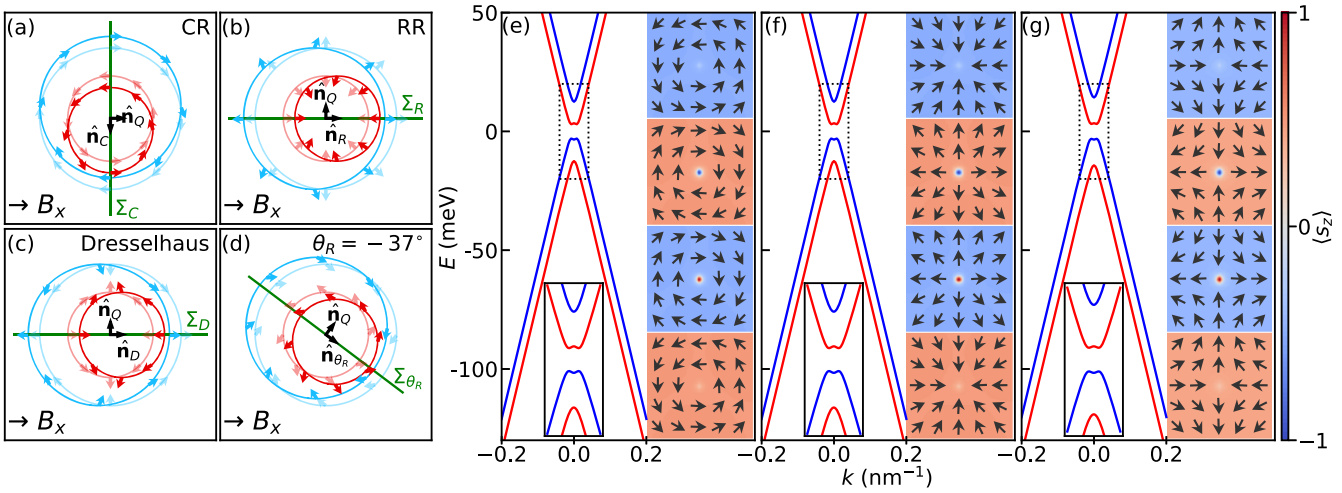

FIG. 1. Left: Schematics of the graphene (2DEG) Fermi contours around the K (Γ) point in the absence (lighter) and presence (solid) of an in-plane magnetic field $\mathbf{B}_\parallel = (B_x, 0, 0)$. The directions $\hat{\mathbf{n}}_{\mathrm{C/R/D}/\theta_\mathrm{R}}$ show how the Fermi contours for different spin textures—(a) CR, (b) RR, (c) Dresselhaus, and (d) canted Rashba SOC with $\theta_\mathrm{R} = -37°$—shift in the k space rendering the spin-Zeeman energy, $\pm g\mu_\mathrm{B}\langle s_x\rangle B_x$. Positions of the mirror planes $\Sigma_{\mathrm{C/R/D}/\theta_\mathrm{R}}$ specify along which transport direction $\hat{\mathbf{n}}_Q \perp \Sigma_\mathrm{SOC}$ one can expect a magnetosymmetry $Q(\hat{\mathbf{n}}_Q, \mathbf{B}_\parallel) = Q(\hat{\mathbf{n}}_Q, -\mathbf{B}_\parallel) = Q(-\hat{\mathbf{n}}_Q, \mathbf{B}_\parallel)$ with respect to a swap of $\mathbf{B}_\parallel$ or $\hat{\mathbf{n}}_Q$. Right: Calculated energy band structures and spin textures near the Dirac point of the proximitized graphene described by $\mathcal{H}_0 + \mathcal{H}_\mathrm{SOC}$, considering (e) $\mathcal{H}_\mathrm{CR+VZ}$, (f) $\mathcal{H}_\mathrm{RR+VZ}$, and (g) $\mathcal{H}_\mathrm{D+VZ}$, in all three cases with $\lambda_\mathrm{VZ} = 3.5$ meV, and separately with $\lambda_\mathrm{CR} = \lambda_\mathrm{RR} = \lambda_\mathrm{D} = 6$ meV in $\mathcal{H}_\mathrm{CR/RR/D}$. The side panels show the spin textures of the spin-split conduction and valence bands—the in-plane black arrows and red-blue color shading are displaying, respectively, $\langle s_x, s_y\rangle$ and $\langle s_z\rangle$, with the latter calibrated by the common color bar at the right of panel (g).

CR (tangential), RR (radial), typical Dresselhaus, and Rashba angle canted SOC spin textures without (lighter) and with (solid) an in-plane magnetic field $\mathbf{B}_\parallel$, exemplified for a special case of $\mathbf{B}_\parallel = (B_x, 0, 0)$. When turning on $\mathbf{B}_\parallel = (B_x, B_y, 0)$ the different SOC textures respond differently, rendering an additional spin-Zeeman interaction $\mathcal{H}_\mathrm{Z} = g\mu_\mathrm{B}\mathbf{s}\cdot\mathbf{B}_\parallel$, where g and μ_B are the g factor and the Bohr magneton, and $\mathbf{s} = (s_x, s_y, s_z)$ is a vector of the 2×2 spin-Pauli matrices. Correspondingly, the initial spin-split Fermi contours (lighter) shift in different directions—for the CR SOC the shifts are along $\hat{\mathbf{n}}_\mathrm{C} \propto \pm(-B_y, B_x, 0)$, i.e., perpendicular to $\mathbf{B}_\parallel$, for the RR SOC they are shifting along $\hat{\mathbf{n}}_\mathrm{R} \propto \pm(B_x, B_y, 0)$, i.e., (anti)parallel to $\mathbf{B}_\parallel$, while for the Dresselhaus SOC the shifts occur along the directions $\hat{\mathbf{n}}_\mathrm{D} \propto \pm(B_x, -B_y, 0)$. Obviously, for a generic $\mathbf{B}_\parallel$ the different types of SOC define different $\hat{\mathbf{n}}_\mathrm{SOC} = \hat{\mathbf{n}}_\mathrm{C/R/D}$. Therefore, when being able to determine a shift direction $\hat{\mathbf{n}}_\mathrm{SOC}$ one would be able to unambiguously determine the type of SOC. As clear from Fig. 1, although the Fermi surfaces shift due to $\mathbf{B}_\parallel$ some of their original mirror symmetries still stay preserved, particularly, the mirror symmetry with respect to the plane $\Sigma_\mathrm{SOC} = \Sigma_\mathrm{C/R/D}$ defined by the corresponding $\hat{\mathbf{n}}_\mathrm{SOC}$ and z vector $\hat{\mathbf{e}}_z = (0, 0, 1)$—note that Σ_SOC stays unaffected when changing the polarity of $\mathbf{B}_\parallel$.

The knob to explore $\hat{\mathbf{n}}_\mathrm{SOC}$ is to rotate an in-plane magnetic field and measure some quantity Q—in a way that does not cause additional shifts of the Fermi contours—along a fixed transport direction $\hat{\mathbf{n}}_Q$. By varying $\mathbf{B}_\parallel$ we vary the Fermi shifts $\hat{\mathbf{n}}_\mathrm{SOC}$ and thus the mirror symmetry planes Σ_SOC of the Fermi contours. Once one finds Σ_SOC such that the mirror of the transport direction $\hat{\mathbf{n}}_Q$ is $-\hat{\mathbf{n}}_Q$, or, equivalently, that $\hat{\mathbf{n}}_Q$ gets perpendicular to $\hat{\mathbf{n}}_\mathrm{SOC}$, see Fig. 1, the quantity Q will experience a magnetosymmetric response $Q(\hat{\mathbf{n}}_Q, \mathbf{B}_\parallel) = Q(\hat{\mathbf{n}}_Q, -\mathbf{B}_\parallel) = Q(-\hat{\mathbf{n}}_Q, \mathbf{B}_\parallel)$ with respect to a swap of the in-plane field or the transport axis. So finding such $\mathbf{B}_\parallel$, and using the above relations connecting its components with those of $\hat{\mathbf{n}}_\mathrm{C/R/D}$, one would be able to determine the type of SOC—CR, RR, or Dresselhaus SOC—as only one of these three vectors $\hat{\mathbf{n}}_\mathrm{C/R/D}$ will be (for a generic $\mathbf{B}_\parallel$) perpendicular to $\hat{\mathbf{n}}_Q$. *Magnetosymmetry of Q probed along $\hat{\mathbf{n}}_Q \perp \hat{\mathbf{n}}_\mathrm{SOC}$ is the robust (topological) feature directly linked to the type of SOC subjected to $\mathbf{B}_\parallel$.* Later, when discussing numerical simulations, we consider Q to be the second conductance peak G_2nd, spin-relaxation rate τ_s^{-1}, and the difference ΔI_c of critical supercurrents, and we fix $\hat{\mathbf{n}}_Q = \hat{\mathbf{e}}_x = (1, 0, 0)$.

The above discussion assumed a system with the spin texture imprinted solely due to either CR, RR, or Dresselhaus SOC, however, the extensions to mixed SOC cases are straightforward. Let us consider the mixed case of CR and RR SOCs, for which the spin texture at any point on the Fermi circle is canted by the Rashba angle θ_R as compared to CR SOC spin texture. By rotating such canted spin texture at any point of the Fermi circle by an in-plane angle $-\theta_\mathrm{R}$, it will turn to tangential, see Fig. 1(d).

Applying the in-plane field $\mathbf{B}_\parallel$ the Fermi contours subjected to such texture will shift along $\hat{\mathbf{n}}_{\mathrm{CR}}(\theta_{\mathrm{R}}) \propto \pm(\sin\theta_{\mathrm{R}} B_x - \cos\theta_{\mathrm{R}} B_y, \sin\theta_{\mathrm{R}} B_y + \cos\theta_{\mathrm{R}} B_x)$—which reduces at $\theta_{\mathrm{R}} = 0$ and $\theta_{\mathrm{R}} = \pi/2$, respectively, to $\hat{\mathbf{n}}_{\mathrm{C}}$ and $\hat{\mathbf{n}}_{\mathrm{R}}$. So, in general, measuring Q along $\hat{\mathbf{n}}_Q$ and varying a direction of the in-plane field, or generically, an angle between the transport direction $\hat{\mathbf{n}}_Q$ and $\mathbf{B}_\parallel$, one can find a sweet-spot angle $\varphi = \sphericalangle(\hat{\mathbf{n}}_Q, \mathbf{B}_\parallel)$ at which $Q(\hat{\mathbf{n}}_Q, \mathbf{B}_\parallel) = Q(\hat{\mathbf{n}}_Q, -\mathbf{B}_\parallel)$ and $\hat{\mathbf{n}}_{\mathrm{CR}}(\theta_{\mathrm{R}}) \perp \hat{\mathbf{n}}_Q$. This sweet-spot angle is related to the Rashba angle as $\theta_{\mathrm{R}} = -\varphi$, up to modulus of adding π.

Although the magnetosymmetric response $Q(\hat{\mathbf{n}}_Q, \mathbf{B}_\parallel) = Q(\hat{\mathbf{n}}_Q, -\mathbf{B}_\parallel)$ is ubiquitously engendered from the underlying spin texture—the concrete Hamiltonians for the proximitized graphene and 2DEG will be provided below—there are two comments to be added. *First*, the more robust the low-energy band structure and spin texture, the less vulnerable is the magnetosymmetry of Q from spectral perturbations that are gaping out the Dirac cones, causing disorder-induced localization and band structure reconstruction [51], deforming circular symmetry, bringing magneto-anisotropies distorting the spin textures, limiting the number of k points by finite size effects, or percolatively "'pinching off" transport channels due to doping inhomogeneities, puddles, coarse grains, rough edges, and so on. As we show later, the magnetosymmetry of proximitized graphene persists even in the case when the Hamiltonian admixes along with the CR, RR, and Dresselhaus SOCs also a nonzero VZ SOC. *Second*, the measurement of Q should be done in a way that is not causing additional shifts of the Fermi contours. Using, for example, a current drive the corresponding electric field $\mathbf{E} = E\hat{\mathbf{n}}_Q$ would shift the Fermi contour momenta by $e\mathbf{E}\tau/\hbar$ (with τ being the transport lifetime) superimposing them with those exerted by $\mathbf{B}_\parallel$, that would require a much refined analysis of getting the Rashba angle. A particular example would be the Rashba-Edelstein effect [52], where the detection of $Q =$ "current-induced magnetization originating from the spin texture" requires an in-plane magnetic field. As both shifts play a role, but the one due to $\mathbf{B}_\parallel$ was omitted in [49], a factor-of-2 discrepancy in an estimation of θ_{R} as compared to DFT [44] can have such a geometrical origin.

To avoid these complications we propose to use transverse magnetic focusing (TMF) [53–60] and the Dyakonov-Perel spin relaxation (DPSR) [61–66]. In the first case, depicted schematically in Fig. 2(a), the Q stands for the second conductance peak $G_{2\mathrm{nd}}$ and $\hat{\mathbf{n}}_Q$ is given by the average direction of carrier propagation, which for cyclotron motion is determined by the edge orientation, the type of the charge carriers (electron or holes) and the polarity of the out-of-plane field $\mathbf{B}_\perp = (0, 0, B_z)$ exerting the Lorentz force. Although the TMF is widely used to explore "topology" and spectral (mini)gaps of the Fermi surface [57,58,60], it is the first conduction peak $G_{1\mathrm{st}}$ that utters to determine such spectral (spin-)splittings. As the latter can be the same for CR and RR in graphene, see the band structures in the right panel in Fig. 1, $G_{1\mathrm{st}}$ itself is not capable of distinguishing the different types of Rashba SOC or their admixture. As we show later by numerical simulations, $G_{2\mathrm{nd}}$ and its magnetosymmetric features [67], $G_{2\mathrm{nd}}(\hat{\mathbf{n}}_Q, \mathbf{B}_\parallel) = G_{2\mathrm{nd}}(\hat{\mathbf{n}}_Q, -\mathbf{B}_\parallel)$, are unique in these regards, so by measuring both, $G_{1\mathrm{st}}$ and $G_{2\mathrm{nd}}$, one gets information about the magnitude and the type of SOC.

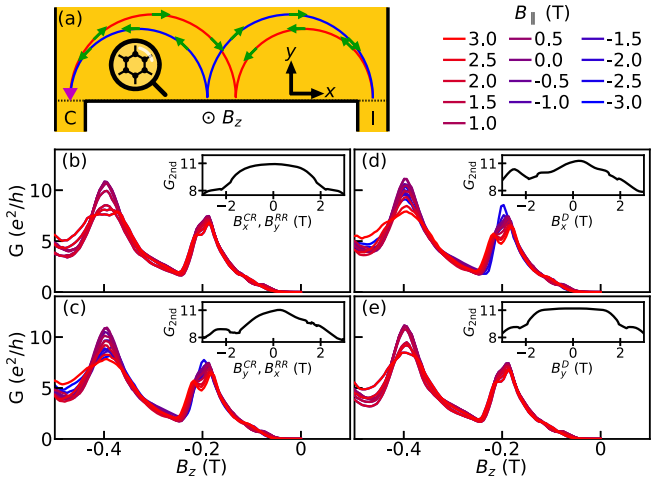

FIG. 2. (a) Three terminal TMF setup with schematics of spin-split skipping orbits and real-space spin textures for RR SOC—the latter come as 90° rotation of the k-space textures displayed in Fig. 1(b). (b)–(e) Simulated conductance between the TMF injector and collector (spaced by 1 μm) as a function of B_z for hole-doped graphene at energy $E = -100$ meV, considering the CR/RR SOC [(b) and (c)], and Dresselhaus SOC [(d) and (e)], all subtended by a varying in-plane magnetic field—B_x^{CR}, B_y^{RR}, and B_x^{D} for the upper panels and B_y^{CR}, B_x^{RR}, and B_y^{D} for the lower panels. As CR and RR Hamiltonians are unitary equivalent, data in (b) and (c) are showing at once two different SOC cases at two differently oriented in-plane fields. Colors code different strengths of $B_\parallel$. The insets show the dependence of the second TMF conductance peaks, $G_{2\mathrm{nd}}$, i.e., G at $B_z \approx -0.4$ T, on the strength of the in-plane magnetic fields.

In the case of DPSR, shown in Fig. 3(a), Q represents the spin-relaxation rate τ_s^{-1} and $\hat{\mathbf{n}}_Q$ is given by the gradient of the nonequilibrium spin accumulation formed between the spin-injecting and spin-extracting electrodes, as inherent to nonlocal spin valve geometries [64,68]. As for the nonmagnetic materials the nonequilibrium spin accumulation does not lead to a spatial imbalance of charges, there are no additional electric field gradients that would shift the Fermi contours. Therefore, in this case the magnetosymmetry of $\tau_s^{-1}(\hat{\mathbf{n}}_Q, \mathbf{B}_\parallel) = \tau_s^{-1}(\hat{\mathbf{n}}_Q, -\mathbf{B}_\parallel)$ should unveil the type of SOC and also its magnitude. Apart from that, it is of pure spintronics nature to know how different types of SOC relax the spin, so in what follows we also quantitatively compare the CR, RR, and Dresselhaus cases.

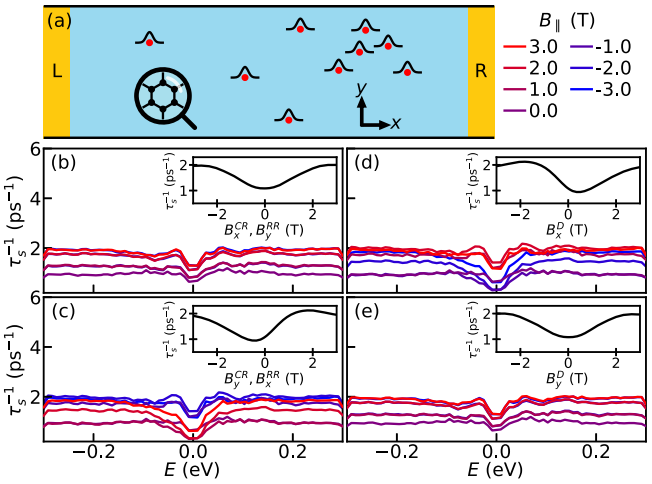

FIG. 3. (a) Two-terminal spin-valve setup with schematics of Gaussian-type disorder. (b)–(e) Simulated DPSR rate as a function of the Fermi energy E for disordered graphene, considering the CR/RR [(b) and (c)], and Dresselhaus SOC [(d) and (e)], all subtended by a varying in-plane magnetic field—B_x^{CR}, B_y^{RR}, and B_x^{D} for the upper panels and B_y^{CR}, B_x^{RR}, and B_y^{D} for the lower panels. As CR and RR Hamiltonians are unitary equivalent, data in (b) and (c) are showing at once two different SOC cases at two differently oriented in-plane fields. Colors code different strengths of the in-plane field. The scattering region is a zigzag ribbon with the width $w = 131a$ and length $L = 300a$, where $a = 2.46$ Å is the graphene lattice constant. The insets show the variation of τ_s^{-1} with the in-plane magnetic fields at $E = 100$ meV.

Model Hamiltonians and their symmetries—The effective tight-binding description of graphene with spin-proximity engendered physics can be modeled by $\mathcal{H} = \mathcal{H}_0 + \mathcal{H}_{\mathrm{Z}} + \mathcal{H}_{\mathrm{SOC}}$. Here, $\mathcal{H}_0 = -t\sum_{\langle m,n\rangle} c_n^\dagger c_m$ represents the graphene nearest-neighbor Hamiltonian with hopping $t = 3$ eV, while $\mathcal{H}_{\mathrm{Z}} = g\mu_{\mathrm{B}}\mathbf{s}\cdot\mathbf{B}$ stands for the spin-Zeeman coupling with the net external magnetic field $\mathbf{B} = \mathbf{B}_\parallel + \mathbf{B}_\perp = (B_x, B_y, B_z) = B_x\hat{\mathbf{e}}_x + B_y\hat{\mathbf{e}}_y + B_z\hat{\mathbf{e}}_z$ and an isotropic g factor for which we use $g = 42.5$—the elevated values of g are typical for the confined graphene-based heterostructures with proximity engineered band splittings [69–71]. Moreover, the out-of-plane component $\mathbf{B}_\perp$, if present, is additionally coupled in all hopping terms by means of the Peierls substitution [72]. The SOC Hamiltonian, $\mathcal{H}_{\mathrm{SOC}}$, comprises VZ, CR, RR, and Dresselhaus SOC terms, which can be, respectively, written in terms of the creation and annihilation operators $c_{m\sigma}^\dagger$ and $c_{m\sigma}$—acting on electron with spin σ on a lattice site m—as

$$\mathcal{H}_{\mathrm{VZ}} = \frac{i}{3\sqrt{3}}\lambda_{\mathrm{VZ}}\sum_{\langle\langle m,n\rangle\rangle}\sum_{\sigma} o(m)c_{n\sigma}^\dagger\nu_{n\leftarrow m}[s_z]_{\sigma\sigma}c_{m\sigma}, \tag{1a}$$

$$\mathcal{H}_{\mathrm{CR}} = \frac{2i}{3}\lambda_{\mathrm{CR}}\sum_{\langle m,n\rangle}\sum_{\sigma,\sigma'} c_{n\sigma}^\dagger[(\mathbf{s}\times\hat{\mathbf{e}}_{n\leftarrow m})\cdot\hat{\mathbf{e}}_z]_{\sigma\sigma'}c_{m\sigma'}, \tag{1b}$$

$$\mathcal{H}_{\mathrm{RR}} = -\frac{2i}{3}\lambda_{\mathrm{RR}}\sum_{\langle m,n\rangle}\sum_{\sigma,\sigma'} c_{n\sigma}^\dagger[\mathbf{s}\cdot\hat{\mathbf{e}}_{n\leftarrow m}]_{\sigma\sigma'}c_{m\sigma'}, \tag{1c}$$

$$\mathcal{H}_{\mathrm{D}} = \frac{2i}{3}\lambda_{\mathrm{D}}\sum_{\langle m,n\rangle}\sum_{\sigma,\sigma'} c_{n\sigma}^\dagger[\mathbf{s}^*\cdot\hat{\mathbf{e}}_{n\leftarrow m}]_{\sigma\sigma'}c_{m\sigma'}. \tag{1d}$$

In Eqs. (1b)–(1d), $\hat{\mathbf{e}}_{n\leftarrow m}$ stands for the unit vector pointing from site m to site n, while $\sum_{\langle m,n\rangle}$ and $\sum_{\langle\langle m,n\rangle\rangle}$ denote summations over all pairs of nearest and second-nearest neighbors.

In the VZ term, Eq. (1a), $m = A, B$ is the sublattice index of site m and $o(A) = 1 = -o(B)$, the sign factor $\nu_{n\leftarrow m}$ is $+1$ (-1) whenever the second-nearest hopping from site m to site n via their common nearest-neighbor forms a clockwise (counterclockwise) path. The Rashba coupling constant λ_{CR} in Eq. (1b), and λ_{RR} in Eq. (1c) can be, alternatively, parametrized by $\lambda_{\mathrm{CR}} = \lambda_{\mathrm{R}}\cos\theta_{\mathrm{R}}$ and $\lambda_{\mathrm{RR}} = \lambda_{\mathrm{R}}\sin\theta_{\mathrm{R}}$, where $\lambda_{\mathrm{R}} > 0$ is the magnitude of Rashba coupling and θ_{R} the Rashba angle. In Eq. (1d), λ_{D} is the Dresselhaus SOC coupling strength, and $\mathbf{s}^* = (s_x, s_y, s_z)^* = (s_x, -s_y, s_z)$. Throughout the main text, we use $\lambda_{\mathrm{CR}} = \lambda_{\mathrm{RR}} = \lambda_{\mathrm{D}} = 6$ meV, close to the recent experiment [46], while λ_{VZ} is either 0 or 3.5 meV, and we vary the components of $\mathbf{B}_\parallel = (B_x, B_y)$ within $[-3, +3]$ T.

The low-energy band structure (centered at the K point of the hexagonal Brillouin zone) of $\mathcal{H}_0 + \mathcal{H}_{\mathrm{SOC}}$ is displayed in Figs. 1(e)–1(g) along with the characteristic spin textures, $\langle\mathbf{s}\rangle = (\langle s_x\rangle, \langle s_y\rangle, \langle s_z\rangle)$, considering for $\mathcal{H}_{\mathrm{SOC}}$, individually, $\mathcal{H}_{\mathrm{CR+VZ}}$, $\mathcal{H}_{\mathrm{RR+VZ}}$, and $\mathcal{H}_{\mathrm{D+VZ}}$ Hamiltonians. As obvious from Figs. 1(e)–1(g), all three cases are spectrally indistinguishable, while the type of SOC fingerprints solely by the spin textures. Assuming $\lambda_{\mathrm{RR}} = \lambda_{\mathrm{CR}}$ it is straightforward to show that the Hamiltonian $\mathcal{H}_0 + \mathcal{H}_{\mathrm{CR+VZ}} + g\mu_{\mathrm{B}}\mathbf{s}\cdot(B_x, B_y, B_z)$ is unitary equivalent to $\mathcal{H}_0 + \mathcal{H}_{\mathrm{RR+VZ}} + g\mu_{\mathrm{B}}\mathbf{s}\cdot(B_y, -B_x, B_z)$ when employing $\mathcal{H} \mapsto U\mathcal{H}U^\dagger$ for U consisting of a $\pi/2$-spin rotation along the z axis, $e^{i\pi/4s_z}$, and $-\pi/2$ corotation of the $\mathbf{B}_\parallel$ field [73]. Generalizing the above argument, any magnetoresponses of graphene with CR + VZ SOC triggered by a magnetic field (B_x, B_y, B_z) are the same as the magnetoproperties of graphene with Rashba angle θ_{R} + VZ SOC in the rotated field $(B_x\cos\theta_{\mathrm{R}} + B_y\sin\theta_{\mathrm{R}}, B_y\cos\theta_{\mathrm{R}} - B_x\sin\theta_{\mathrm{R}}, B_z)$. The case of the Dresselhaus SOC is more peculiar as it requires to change the sign of VZ SOC, namely, assuming $\lambda_{\mathrm{D}} = \lambda_{\mathrm{CR}}$, $\mathcal{H}_0 + \mathcal{H}_{\mathrm{CR+VZ}} + g\mu_{\mathrm{B}}\mathbf{s}\cdot(B_x, B_y, B_z)$ is antiunitary [74], $\mathcal{H} \mapsto U\mathcal{H}^*U^\dagger$, equivalent to $\mathcal{H}_0 + \mathcal{H}_{\mathrm{D-VZ}} + g\mu_{\mathrm{B}}\mathbf{s}\cdot(B_y, B_x, B_z)$ when employing U consisting of a $-\pi/2$-spin rotation along the z-axis, $e^{-i\pi/4s_z}$, and mirroring the $\mathbf{B}_\parallel$ field along the $y = x$ axis.

Numerical results: TMF and DPSR—To corroborate the three types of SOC with the magnetosymmetry responses of TMF ($G_{2\mathrm{nd}}$) and DPSR (τ_s^{-1}) when swapping $\mathbf{B}_\parallel \mapsto -\mathbf{B}_\parallel$, we performed bench marking large-scale

[75–78] magnetotransport simulations. By incorporating $\mathcal{H}_0 + \mathcal{H}_Z + \mathcal{H}_{SOC}$ within the transport package Kwant [79] and by varying the Fermi energy, SOC strengths/types, disorder, and magnetic field, we explicitly verify the validity of all of our phenomenological predictions about $Q(\hat{\mathbf{n}}_Q, \mathbf{B}_\parallel) = Q(\hat{\mathbf{n}}_Q, -\mathbf{B}_\parallel)$ for $Q = G_{2nd}$ and τ_s^{-1} [panels (b) and (e) in Figs. 2 and 3], fixing the transport axis $\hat{\mathbf{n}}_Q$ along the zigzag $\hat{\mathbf{e}}_x$ direction. We explicitly show that for CR SOC, $Q(\hat{\mathbf{e}}_x, B_x\hat{\mathbf{e}}_x) = Q(\hat{\mathbf{e}}_x, -B_x\hat{\mathbf{e}}_x)$, while for RR and Dresselhaus SOC, $Q(\hat{\mathbf{e}}_x, B_y\hat{\mathbf{e}}_y) = Q(\hat{\mathbf{e}}_x, -B_y\hat{\mathbf{e}}_y)$, in accordance with the above (anti)unitary equivalences and geometrical reasoning. Moreover, in the case when CR and RR are mixed via θ_R, $Q(\hat{\mathbf{e}}_x, \mathbf{B}_\parallel) = Q(\hat{\mathbf{e}}_x, -\mathbf{B}_\parallel)$ if $\sphericalangle(\hat{\mathbf{e}}_x, \mathbf{B}_\parallel) = -\theta_R(+\pi)$.

TMF—Figure 2 shows the conductance G as a function of $B_z \in [-0.5, 0]$ T for a symmetric three-terminal TMF setup schematically shown in Fig. 2(a), with proximity-induced CR/RR [panels (b) and (c)] and Dresselhaus [panels (d) and (e)] SOC. Results are displayed for the hole-doped graphene at energy $E = -100$ meV; for corresponding figures with $\lambda_{VZ} \neq 0$, different values of E, λ_{CR}, λ_{RR}, and λ_D and also disorders, see the Supplemental Material [80]. The insets in each panel show variations of the second conductance peak, $G_{2nd}(\hat{\mathbf{e}}_x, \mathbf{B}_\parallel)$, with either $\mathbf{B}_\parallel = B_x\hat{\mathbf{e}}_x$ or $B_y\hat{\mathbf{e}}_y$ displaying the expected magnetosymmetries correlated with the given type of SOC. In weaker in-plane fields, $|\mathbf{B}_\parallel| \lesssim 1$ T, G_{2nd} shows no pronounced variations, but at higher fields the variations can approach up to 30% what offers a sizable experimental signal.

DPSR—Figure 3 shows the simulated DPSR rates, τ_s^{-1}, as functions of the Fermi energy $E \in [-0.3, +0.3]$ eV for a symmetric two-terminal setup, schematically shown in Fig. 3(a), considering CR/RR [panels (b) and (c)], and Dresselhaus [panels (d) and (e)] SOC, in the presence of nonmagnetic on-site disorder; electrons are injected from the leads and carry out-of-plane spin polarization. DPSR is calculated following the methodology developed in Refs. [91–93] for a nonmagnetic spatially correlated Gaussian [94] with an effective impurity concentration $\eta = 0.799\%$. Insets show $\tau_s^{-1}(\hat{\mathbf{e}}_x, \mathbf{B}_\parallel)$ at $E = 100$ meV, with expected magnetosymmetries [panels (b) and (e)] correlated with the type of SOC. As a consequence of the (anti)unitarity, CR and RR SOC, but also Dresselhaus SOC do not lead to substantially different qualitative spin-relaxation profiles when varying the Fermi level, neither to an unusual spin relaxation anisotropy of τ_s^{-1}-in-plane vs τ_s^{-1}-out-of-plane spin-relaxation rates.

Radial SDE—Finally, let us offer a short perspective how engendering exotic RR SOC in a superconducting 2DEG would manifest in the SDE. Considering the quadratic 2DEG dispersion set by an effective mass m^* and Fermi energy E in the presence of RR SOC, $\alpha_{RR}(k_x s_x + k_y s_y)$, and an additional Zeeman coupling, $\mathcal{H}_Z$, due to the in-plane field $\mathbf{B}_\parallel$, the Fermi contours acquire longitudinal shifts along $\mathbf{B}_\parallel$; see Fig. 1(b). Turning on the superconducting correlations the 2DEG will develop the helical phase, $\psi_{RR}(\mathbf{r}) = e^{i\mathbf{P}_{RR}\cdot\mathbf{r}/\hbar}|\psi|$, with a finite center of mass momentum, $\mathbf{P}_{RR} \propto g\mu_B\alpha_{RR}(m^*/\hbar E)\mathbf{B}_\parallel$, aligned along $\mathbf{B}_\parallel$. This opposes the CR case [97–104], $\alpha_{CR}(k_x s_y - k_y s_x)$, where the center of mass momentum, $\mathbf{P}_{CR}$, develops in the direction perpendicular to $\mathbf{B}_\parallel$, i.e., $\psi_{CR}(\mathbf{r}) = e^{i\mathbf{P}_{CR}\cdot\mathbf{r}/\hbar}|\psi|$, with $\mathbf{P}_{CR} \propto g\mu_B\alpha_{CR}(m^*/\hbar E)(\mathbf{B}_\parallel \times \hat{\mathbf{e}}_z)$. The immediate ramifications lead to different magnetochiral responses of the SDE critical current, I^c_{SDE}, see Fig. 4, and of the Josephson inductance, L_J, on a direction of probing current $\mathbf{j} \propto \hat{\mathbf{n}}_Q$ and the in-plane field $\mathbf{B}_\parallel$. So both, $I^c_{SDE} = I^c_0 + \gamma_I f(\mathbf{j}, \mathbf{B}_\parallel)$ and $L_J = L_{J0} + \gamma_L f(\mathbf{j}, \mathbf{B}_\parallel)$, will depend on the magnetochiral factor $f(\mathbf{j}, \mathbf{B}_\parallel)$ that, correspondingly, for RR or CR SOC equals to $\mathbf{j}\cdot\mathbf{B}_\parallel$ and $\mathbf{j}\cdot(\mathbf{B}_\parallel \times \hat{\mathbf{e}}_z)$ [103,105–108]; the magnetochiral coefficients $\gamma_{I/L}$ encapsulate all material dependencies accompanying currents and inductances. This unique magnetochiral feature offered by RR SOC, if possible to realize in a 2DEG, would allow to unveil unprecedentedly the origin of SDE, particularly, its SOC or inhomogenous Meissner-screening roots.

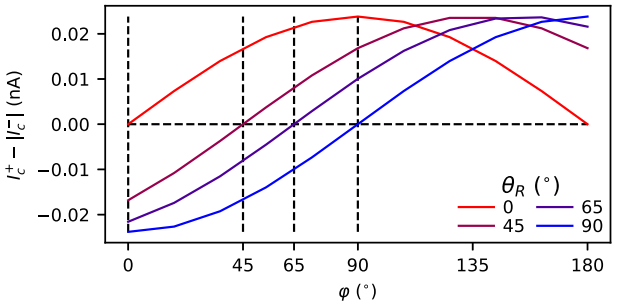

FIG. 4. Simulated SDE, $\Delta I_c = I_c^+ - |I_c^-|$, as a function of the angle $\varphi = \sphericalangle(\hat{\mathbf{e}}_x, \mathbf{B}_\parallel) \in [0, \pi]$ for a 2DEG-based Josephson junction held at three different Rashba angles θ_R, corresponding to CR (red), RR (blue), and mixed (violet) situations. As a hallmark of the SDE, $\Delta I_c = Q(\hat{\mathbf{e}}_x, \mathbf{B}_\parallel)$ gets its absolute maxima at $\varphi = -\theta_R(+\pi)$, while it turns to zero at $\theta_R(+\pi)$. For the details of simulation and parameters, see Supplemental Material [80].

Conclusions—Although spectrally the CR, RR, and Dresselhaus SOC manifest similarly, the underlying wave functions and spin textures discern when exposed to in-plane magnetic field. We showed that the emergent spin-orbit physics can be scrutinized by means of the magnetotransport symmetries of TMF and DPSR. Even though we primarily focused on graphene with the proximity engendered SOC, we predict that the superconducting 2DEG with the induced RR SOC would display a fully novel radial magnetochiral response that can ultimately unveil physics behind the SDE, namely, its SOC-prompt or diamagnetic origins.

Acknowledgments—We thank Jaroslav Fabian and Paulo E. Faria Junior for useful discussions. W.-H. K., A. G.-R.,

and M.-H. L. acknowledge National Science and Technology Council of Taiwan (Grant No. NSTC 112-2112-M-006-019-MY3) for financial support and National Center for High-performance Computing (NCHC) for providing computational and storage resources. M. B. acknowledges support by the Deutsche Forschungsgemeinschaft (DFG, German Research Foundation) within the Collaborative Research Center SFB 1277 (Project-ID 314695032, subproject A07). A. C. acknowledges funding by Deutsche Forschungsgemeinschaft (DFG; German Research Foundation) within the Research grant "Spin and magnetic properties of superconducting tunnel junctions" (Project-ID 454646522) and the Collaborative Research Center SFB 1277 (Project-ID 314695032, subproject B07). A. M.-K. acknowledges partial support by program "Excellence initiative—research university" for the AGH University of Krakow, and by Polish high-performance computing infrastructure PLGrid (HPC Center: ACK Cyfronet AGH) for providing computer facilities and support within computational Grant No. PLG/2023/016561. D. K. acknowledges partial support from the Project No. IM-2021-26 (SUPERSPIN) funded by the Slovak Academy of Sciences via the programme IMPULZ 2021, and Grant DESCOM VEGA 2/0183/21.

[1] W. Han, R. K. Kawakami, M. Gmitra, and J. Fabian, Nat. Nanotechnol. **9**, 794 (2014).
[2] S. Roche, J. Åkerman, B. Beschoten, J.-C. Charlier, M. Chshiev, S. P. Dash, B. Dlubak, J. Fabian, A. Fert, M. Guimaraes, F. Guinea, I. Grigorieva, C. Schönenberger, P. Seneor, C. Stampfer, S. O. Valenzuela, X. Waintal, and B. van Wees, 2D Mater. **2**, 030202 (2015).
[3] I. Žutić, A. Matos-Abiague, B. Scharf, H. Dery, and K. Belashchenko, Mater. Today **22**, 85 (2019).
[4] A. Avsar, H. Ochoa, F. Guinea, B. Özyilmaz, B. J. van Wees, and I. J. Vera-Marun, Rev. Mod. Phys. **92**, 021003 (2020).
[5] J. F. Sierra, J. Fabian, R. K. Kawakami, S. Roche, and S. O. Valenzuela, Nat. Nanotechnol. **16**, 856 (2021).
[6] Y. Cao, V. Fatemi, S. Fang, K. Watanabe, T. Taniguchi, E. Kaxiras, and P. Jarillo-Herrero, Nature (London) **556**, 43 (2018).
[7] D. M. Kennes, M. Claassen, L. Xian, A. Georges, A. J. Millis, J. Hone, C. R. Dean, D. N. Basov, A. N. Pasupathy, and A. Rubio, Nat. Phys. **17**, 155 (2021).
[8] J.-X. Lin, Y.-H. Zhang, E. Morissette, Z. Wang, S. Liu, D. Rhodes, K. Watanabe, T. Taniguchi, J. Hone, and J. I. A. Li, Science **375**, 437 (2022).
[9] K. Szałowski, M. Milivojević, D. Kochan, and M. Gmitra, 2D Mater. **10**, 025013 (2023).
[10] C. L. Tschirhart, E. Redekop, L. Li, T. Li, S. Jiang, T. Arp, O. Sheekey, T. Taniguchi, K. Watanabe, M. E. Huber, K. F. Mak, J. Shan, and A. F. Young, Nat. Phys. **19**, 807 (2023).
[11] A. Garcia-Ruiz, V. Enaldiev, A. McEllistrim, and V. I. Fal'ko, Nano Lett. **23**, 4120 (2023).
[12] Z. Tao, B. Shen, W. Zhao, N. C. Hu, T. Li, S. Jiang, L. Li, K. Watanabe, T. Taniguchi, A. H. MacDonald, J. Shan, and K. F. Mak, Nat. Nanotechnol. **19**, 28 (2024).
[13] M. Gmitra, S. Konschuh, C. Ertler, C. Ambrosch-Draxl, and J. Fabian, Phys. Rev. B **80**, 235431 (2009).
[14] S. Konschuh, M. Gmitra, D. Kochan, and J. Fabian, Phys. Rev. B **85**, 115423 (2012).
[15] C. Weeks, J. Hu, J. Alicea, M. Franz, and R. Wu, Phys. Rev. X **1**, 021001 (2011).
[16] M. Gmitra, D. Kochan, and J. Fabian, Phys. Rev. Lett. **110**, 246602 (2013).
[17] T. P. Kaloni, L. Kou, T. Frauenheim, and U. Schwingenschlögl, Appl. Phys. Lett. **105**, 233112 (2014).
[18] Z. Wang, D.-K. Ki, H. Chen, H. Berger, A. H. MacDonald, and A. F. Morpurgo, Nat. Commun. **6**, 8339 (2015).
[19] S. Irmer, T. Frank, S. Putz, M. Gmitra, D. Kochan, and J. Fabian, Phys. Rev. B **91**, 115141 (2015).
[20] F. Calleja, H. Ochoa, M. Garnica, S. Barja, J. J. Navarro, A. Black, M. M. Otrokov, E. V. Chulkov, A. Arnau, A. L. Vázquez de Parga, F. Guinea, and R. Miranda, Nat. Phys. **11**, 43 (2015).
[21] M. Gmitra, D. Kochan, P. Högl, and J. Fabian, Phys. Rev. B **93**, 155104 (2016).
[22] A. M. Alsharari, M. M. Asmar, and S. E. Ulloa, Phys. Rev. B **94**, 241106 (2016).
[23] Z. Wang, D.-K. Ki, J. Y. Khoo, D. Mauro, H. Berger, L. S. Levitov, and A. F. Morpurgo, Phys. Rev. X **6**, 041020 (2016).
[24] K. Zollner, T. Frank, S. Irmer, M. Gmitra, D. Kochan, and J. Fabian, Phys. Rev. B **93**, 045423 (2016).
[25] M. Gmitra, D. Kochan, P. Högl, and J. Fabian, in *Spin Orbitronics and Topological Properties of Nanostructures* (World Scientific, Singapore, 2018), pp. 18–39.
[26] T. Frank, S. Irmer, M. Gmitra, D. Kochan, and J. Fabian, Phys. Rev. B **95**, 035402 (2017).
[27] D. Kochan, S. Irmer, and J. Fabian, Phys. Rev. B **95**, 165415 (2017).
[28] T. Völkl, T. Rockinger, M. Drienovsky, K. Watanabe, T. Taniguchi, D. Weiss, and J. Eroms, Phys. Rev. B **96**, 125405 (2017).
[29] K. Zollner, M. Gmitra, and J. Fabian, New J. Phys. **20**, 073007 (2018).
[30] S. Zihlmann, A. W. Cummings, J. H. Garcia, M. Kedves, K. Watanabe, T. Taniguchi, C. Schönenberger, and P. Makk, Phys. Rev. B **97**, 075434 (2018).
[31] T. Völkl, D. Kochan, T. Ebnet, S. Ringer, D. Schiermeier, P. Nagler, T. Korn, C. Schüller, J. Fabian, D. Weiss, and J. Eroms, Phys. Rev. B **99**, 085401 (2019).
[32] T. S. Ghiasi, A. A. Kaverzin, P. J. Blah, and B. J. van Wees, Nano Lett. **19**, 5959 (2019).
[33] C. K. Safeer, J. Ingla-Aynés, N. Ontoso, F. Herling, W. Yan, L. E. Hueso, and F. Casanova, Nano Lett. **20**, 4573 (2020).
[34] L. A. Benítez, W. Savero Torres, J. F. Sierra, M. Timmermans, J. H. Garcia, S. Roche, M. V. Costache, and S. O. Valenzuela, Nat. Mater. **19**, 170 (2020).
[35] J. Ingla-Aynés, F. Herling, J. Fabian, L. E. Hueso, and F. Casanova, Phys. Rev. Lett. **127**, 047202 (2021).
[36] P. Tiwari, M. K. Jat, A. Udupa, D. S. Narang, K. Watanabe, T. Taniguchi, D. Sen, and A. Bid, npj 2D Mater. Appl. **6**, 1 (2022).

[37] N. Ontoso, C. K. Safeer, F. Herling, J. Ingla-Aynés, H. Yang, Z. Chi, B. Martin-Garcia, I. n. Robredo, M. G. Vergniory, F. de Juan, M. Reyes Calvo, L. E. Hueso, and F. Casanova, Phys. Rev. Appl. **19**, 014053 (2023).

[38] A. W. Cummings, J. H. Garcia, J. Fabian, and S. Roche, Phys. Rev. Lett. **119**, 206601 (2017).

[39] M. Offidani, M. Milletarì, R. Raimondi, and A. Ferreira, Phys. Rev. Lett. **119**, 196801 (2017).

[40] Y. Li and M. Koshino, Phys. Rev. B **99**, 075438 (2019).

[41] A. David, P. Rakyta, A. Kormányos, and G. Burkard, Phys. Rev. B **100**, 085412 (2019).

[42] T. Naimer, K. Zollner, M. Gmitra, and J. Fabian, Phys. Rev. B **104**, 195156 (2021).

[43] A. Veneri, D. T. S. Perkins, C. G. Péterfalvi, and A. Ferreira, Phys. Rev. B **106**, L081406 (2022).

[44] S. Lee, D. J. P. de Sousa, Y.-K. Kwon, F. de Juan, Z. Chi, F. Casanova, and T. Low, Phys. Rev. B **106**, 165420 (2022).

[45] C. G. Péterfalvi, A. David, P. Rakyta, G. Burkard, and A. Kormányos, Phys. Rev. Res. **4**, L022049 (2022).

[46] L. Sun, L. Rademaker, D. Mauro, A. Scarfato, Á. Pásztor, I. Gutiérrez-Lezama, Z. Wang, J. Martinez-Castro, A. F. Morpurgo, and C. Renner, Nat. Commun. **14**, 3771 (2023).

[47] T. Frank, P. E. Faria Junior, K. Zollner, and J. Fabian, Phys. Rev. B **109**, L241403 (2024).

[48] K. Zollner, S. a. M. João, B. K. Nikolić, and J. Fabian, Phys. Rev. B **108**, 235166 (2023).

[49] H. Yang, B. Martin-Garcia, J. Kimák, E. Schmoranzerová, E. Dolan, Z. Chi, M. Gobbi, P. Němec, L. E. Hueso, and F. Casanova, Nat. Mater. (2024), 10.1038/s41563-024-01985-y.

[50] G. Dresselhaus, Phys. Rev. **100**, 580 (1955).

[51] Y. G. Pogorelov, V. M. Loktev, and D. Kochan, Phys. Rev. B **102**, 155414 (2020).

[52] V. Edelstein, Solid State Commun. **73**, 233 (1990).

[53] H. van Houten, C. W. J. Beenakker, J. G. Williamson, M. E. I. Broekaart, P. H. M. van Loosdrecht, B. J. van Wees, J. E. Mooij, C. T. Foxon, and J. J. Harris, Phys. Rev. B **39**, 8556 (1989).

[54] V. S. Tsoi, J. Bass, and P. Wyder, Rev. Mod. Phys. **71**, 1641 (1999).

[55] T. Taychatanapat, K. Watanabe, T. Taniguchi, and P. Jarillo-Herrero, Nat. Phys. **9**, 225 (2013).

[56] M. Beconcini, S. Valentini, R. Krishna Kumar, G. H. Auton, A. K. Geim, L. A. Ponomarenko, M. Polini, and F. Taddei, Phys. Rev. B **94**, 115441 (2016).

[57] M. Kohda, T. Okayasu, and J. Nitta, Sci. Rep. **9**, 1909 (2019).

[58] A. I. Berdyugin, B. Tsim, P. Kumaravadivel, S. G. Xu, A. Ceferino, A. Knothe, R. Krishna Kumar, T. Taniguchi, K. Watanabe, A. K. Geim, I. V. Grigorieva, and V. I. Fal'ko, Sci. Adv. **6**, eaay7838 (2020).

[59] M. J. Rendell, S. D. Liles, A. Srinivasan, O. Klochan, I. Farrer, D. A. Ritchie, and A. R. Hamilton, Phys. Rev. B **107**, 045304 (2023).

[60] I. Klanurak, K. Watanabe, T. Taniguchi, S. Chatraphorn, and T. Taychatanapat, Nano Lett. **24**, 6330 (2024).

[61] M. I. D'yakonov and V. I. Perel', Phys. Lett. **35A**, 459 (1971).

[62] M. I. D'yakonov and V. I. Perel', Sov. Phys. Solid State, USSR **13**, 3023 (1972).

[63] F. Meier and B. P. Zakharchenya, *Optical Orientation (Modern Problems in Condensed Matter Sciences Vol. 8)* (Elsevier, Amsteradm, 1984).

[64] J. Fabian, A. Matos-Abiague, C. Ertler, P. Stano, and I. Žutić, Acta Phys. Slovaca **57**, 565 (2007).

[65] P. Boross, B. Dóra, A. Kiss, and F. Simon, Sci. Rep. **3**, 3233 (2013).

[66] Evgeny Y. Tsymbal and I. Žutić, *Spintronics Handbook: Spin Transport and Magnetism)* (CRC Press, Boca Raton, 2021).

[67] We focus on the second conductance TMF peak, because there two skipping orbits of the spin-split Fermi contour coalesce, see schematics in Fig. 2(a), what contrasts the first TMF peak that is becoming spin-split at elevated values of $\lambda_{\mathrm{CR/RR/D}}$'s or at larger in-plane magnetic/Zeeman fields—see Fig. 2 and also SM. Similarly, the higher TMF peaks are suffering from a more pronounced smearing—a finite width of Injector allows for an injection of electrons with varying incidence angles, while this variation grows with a propagation time, and with a bouncing of the skipping orbits off the edge the final signal gets more smeared. It shall be emphasized that our results about the non-spin-split second TMF peak are valid assuming the Rashba and Dresselhaus SOC terms dominate over the in-plane Zeeman coupling, in the opposite case, the spin-textures of the skipping orbits and the Fermi contours subordinate to $\mathcal{H}_Z$.

[68] N. Tombros, C. Jozsa, M. Popinciuc, H. T. Jonkman, and B. J. van Wees, Nature (London) **448**, 571 (2007).

[69] T. Frank and J. Fabian, Phys. Rev. B **102**, 165416 (2020).

[70] Z. Ge, S. Slizovskiy, P. Polizogopoulos, T. Joshi, T. Taniguchi, K. Watanabe, D. Lederman, V. I. Fal'ko, and J. Velasco, Nat. Nanotechnol. **18**, 250 (2023).

[71] F. Xiang, A. Gupta, A. Chaves, Z. E. Krix, K. Watanabe, T. Taniguchi, M. S. Fuhrer, F. M. Peeters, D. Neilson, M. V. Milošević, and A. R. Hamilton, Nano Lett. **23**, 9683 (2023).

[72] J. M. Luttinger, Phys. Rev. **84**, 814 (1951).

[73] We thank the anonymous referee for bringing this unitary equivalence point of view.

[74] Other way to see that is to say that CR + VZ SOC in (B_x, B_y, B_z)-field at K point, is equivalent to CR + VZ SOC in the (B_y, B_x, B_z) field at K' point. As we work in the real-space tight-binding representation we do not pursue this point of view.

[75] M.-H. Liu, P. Rickhaus, P. Makk, E. Tóvári, R. Maurand, F. Tkatschenko, M. Weiss, C. Schönenberger, and K. Richter, Phys. Rev. Lett. **114**, 036601 (2015).

[76] P. Rickhaus, P. Makk, M.-H. Liu, E. Tóvári, M. Weiss, R. Maurand, K. Richter, and C. Schönenberger, Nat. Commun. **6**, 6470 (2015).

[77] A. Mreńca-Kolasińska, S.-C. Chen, and M.-H. Liu, npj 2D Mater. Appl. **7**, 1 (2023).

[78] Q. Rao, W.-H. Kang, H. Xue, Z. Ye, X. Feng, K. Watanabe, T. Taniguchi, N. Wang, M.-H. Liu, and D.-K. Ki, Nat. Commun. **14**, 6124 (2023).

[79] C. W. Groth, M. Wimmer, A. R. Akhmerov, and X. Waintal, New J. Phys. **16**, 063065 (2014).
[80] See Supplemental Material at http://link.aps.org/supplemental/10.1103/PhysRevLett.133.216201 for further calculational details about TMF and DPSR, and also for the corresponding results valid for other parameter regimes, which includes Refs. [81–90].
[81] A. Eckmann, A. Felten, A. Mishchenko, L. Britnell, R. Krupke, K. S. Novoselov, and C. Casiraghi, Nano Lett. **12**, 3925 (2012).
[82] X. Xu, L. F. C. Pereira, Y. Wang, J. Wu, K. Zhang, X. Zhao, S. Bae, C. Tinh Bui, R. Xie, J. T. L. Thong, B. H. Hong, K. P. Loh, D. Donadio, B. Li, and B. Ozyilmaz, Nat. Commun. **5**, 3689 (2014).
[83] H. G. Kim, K. D. Kihm, W. Lee, G. Lim, S. Cheon, W. Lee, K. R. Pyun, S. H. Ko, and S. Shin, Carbon **125**, 39 (2017).
[84] P. G. De Gennes, *Superconductivity of Metals and Alloys* (Addison Wesley, Redwood City, 1989).
[85] I. Vurgaftman, J. R. Meyer, and L. R. Ram-Mohan, J. Appl. Phys. **89**, 5815 (2001).
[86] C. Baumgartner, L. Fuchs, L. Frész, S. Reinhardt, S. Gronin, G. C. Gardner, M. J. Manfra, N. Paradiso, and C. Strunk, Phys. Rev. Lett. **126**, 037001 (2021).
[87] W. Mayer, W. F. Schiela, J. Yuan, M. Hatefipour, W. L. Sarney, S. P. Svensson, A. C. Leff, T. Campos, K. S. Wickramasinghe, M. C. Dartiailh, I. Žutić, and J. Shabani, ACS Appl. Electron. Mater. **2**, 2351 (2020).
[88] R. M. Seraide and G.-Q. Hai, Braz. J. Phys. **32**, 344 (2002).
[89] V. P. Ostroukh, B. Baxevanis, A. R. Akhmerov, and C. W. J. Beenakker, Phys. Rev. B **94**, 094514 (2016).
[90] K. Zuo, V. Mourik, D. B. Szombati, B. Nijholt, D. J. van Woerkom, A. Geresdi, J. Chen, V. P. Ostroukh, A. R. Akhmerov, S. R. Plissard, D. Car, E. P. Bakkers, D. I. Pikulin, L. P. Kouwenhoven, and S. M. Frolov, Phys. Rev. Lett. **119**, 187704 (2017).
[91] J. Bundesmann, D. Kochan, F. Tkatschenko, J. Fabian, and K. Richter, Phys. Rev. B **92**, 081403 (2015).
[92] D. Kochan, M. Barth, A. Costa, K. Richter, and J. Fabian, Phys. Rev. Lett. **125**, 087001 (2020).
[93] M. Barth, J. Fuchs, and D. Kochan, Phys. Rev. B **105**, 205409 (2022).
[94] Disorder is generated by means of the Thorsos-Monte-Carlo method [95] and is defined by the on-site potential–on-site potential correlation function $C(|\mathbf{r}-\mathbf{r}'|)^{2D} = \langle U(\mathbf{r}), U(\mathbf{r}')\rangle = K_0[(\hbar v_F)^2/2\pi\xi^2]\exp[-(|\mathbf{r}-\mathbf{r}'|^2/2\xi^2)]$, as already used in other Dirac systems [96]. The parameter ξ is the spatial correlation length, $\xi = 10a$, such that effective impurity concentration $\eta = (\pi\xi^2/wL) = 0.799\%$. Furthermore, K_0 is a dimensionless scaling parameter which is set to 0.1, and we define Fermi velocity v_F such that $\hbar(v_F/a) = (\sqrt{3}/2)t$ where $t = 3$ eV. Finally, we introduce periodic boundary conditions in a direction perpendicular to the transport axis, where we include a phase factor $\exp(i\phi)$ analogously to Refs. [91–93]. The spin-flip relaxation rates are then obtained by averaging over 20 phases $\phi \in [0, 2\pi]$ and 30 different disorder configurations.
[95] C. A. Mack, Appl. Opt. **52**, 1472 (2013).
[96] J. Dufouleur, E. Xypakis, B. Büchner, R. Giraud, and J. H. Bardarson, Phys. Rev. B **97**, 075401 (2018).
[97] V. M. Edelshtein, Sov. Phys.—JETP **68**, 1244 (1989).
[98] A. Daido, Y. Ikeda, and Y. Yanase, Phys. Rev. Lett. **128**, 037001 (2022).
[99] N. F. Q. Yuan and L. Fu, Proc. Natl. Acad. Sci. U.S.A. **119**, e2119548119 (2022).
[100] J. J. He, Y. Tanaka, and N. Nagaosa, New J. Phys. **24**, 053014 (2022).
[101] S. Ilić and F. S. Bergeret, Phys. Rev. Lett. **128**, 177001 (2022).
[102] M. Davydova, S. Prembabu, and L. Fu, Sci. Adv. **8**, eabo0309 (2022).
[103] D. Kochan, A. Costa, I. Zhumagulov, and I. Žutić, arXiv:2303.11975.
[104] A. Banerjee, M. Geier, M. A. Rahman, C. Thomas, T. Wang, M. J. Manfra, K. Flensberg, and C. M. Marcus, Phys. Rev. Lett. **131**, 196301 (2023).
[105] C. Baumgartner, L. Fuchs, A. Costa, S. Reinhardt, S. Gronin, G. C. Gardner, T. Lindemann, M. J. Manfra, P. E. Faria Junior, D. Kochan, J. Fabian, N. Paradiso, and C. Strunk, Nat. Nanotechnol. **17**, 39 (2022).
[106] C. Baumgartner, L. Fuchs, A. Costa, J. Picó-Cortés, S. Reinhardt, S. Gronin, G. C. Gardner, T. Lindemann, M. J. Manfra, P. E. Faria Junior, D. Kochan, J. Fabian, N. Paradiso, and C. Strunk, J. Phys. Condens. Matter **34**, 154005 (2022).
[107] A. Costa, C. Baumgartner, S. Reinhardt, J. Berger, S. Gronin, G. C. Gardner, T. Lindemann, M. J. Manfra, J. Fabian, D. Kochan, N. Paradiso, and C. Strunk, Nat. Nanotechnol. **18**, 1266 (2023).
[108] A. Costa, J. Fabian, and D. Kochan, Phys. Rev. B **108**, 054522 (2023).